

# Mean-Field Ring Polymer Rates Using a Population Dividing Surface

Nathan London,<sup>†,‡</sup> Siyu Bu,<sup>†</sup> Britta Johnson,<sup>†,¶</sup> and Nandini Ananth<sup>\*,†</sup>

<sup>†</sup>*Department of Chemistry, Cornell University, Ithaca, NY*

<sup>‡</sup>*Current address: Division of Energy, Matter and Systems, School of Science and  
Engineering, University of Missouri-Kansas City, Kansas City, MO*

<sup>¶</sup>*Current address: Physical Science Division, Pacific Northwest National Laboratory*

E-mail: ananth@cornell.edu

## Abstract

Mean-field Ring Polymer Molecular Dynamics (MF-RPMD) offers a computationally efficient method for the simulation of reaction rates in multi-level systems. Previous work has established that, to model a nonadiabatic state-to-state reaction accurately, the dividing surface must be chosen to explicitly sample kinked ring polymer configurations where at least one bead is in a different electronic state than the others. Building on this, we introduce a population difference coordinate and a kink-constrained dividing surface, and we test the accuracy of the resulting mean-field rate theory on a series of linear vibronic coupling model systems as well as spin-boson models. We demonstrate that this new MF-RPMD rate approach is efficient to implement and quantitatively accurate for models over a wide range of driving forces, coupling strengths, and temperatures.

## Introduction

Nonadiabatic condensed phase reactions play a critical role in understanding reaction mechanisms for a range of interesting systems including proton coupled electron transfer in biological systems and charge transfer in energetic materials.<sup>1-6</sup> Despite the development of numerous nonadiabatic dynamic methods for the characterization of reaction rates and mechanisms, atomistic simulations of multi-level systems that incorporate nuclear quantum effects and vibronic couplings remain largely out of reach.

Perhaps the most ubiquitous and successful nonadiabatic rate theory is the Marcus theory for electron transfer that assumes a classical solvent.<sup>7</sup> Going beyond Marcus theory, Fermi's Golden Rule (FGR) rate theory incorporates nuclear quantum effects, and can be computed exactly for parabolic potentials. In certain regimes, FGR rates can be approximated using Wolynes rate theory,<sup>8</sup> and limitations of the Wolynes approach have been addressed by recent work, extending the methods applicability to the Marcus inverted regime and improving its accuracy for high temperatures and anharmonic potentials.<sup>9-13</sup> Despite these advances, these

theories are confined to the weak perturbation limit where FGR is applicable, although an interpolation strategy has been proposed to move between the golden-rule limit theories and adiabatic rate theory approaches.<sup>14</sup>

Dynamical methods developed to study the mechanisms of nonadiabatic processes and to compute rate constants include exact methods like MultiConfiguration Time-Dependent Hartree (MCTDH)<sup>15,16</sup> real-time path-integral based approaches,<sup>17-19</sup> and Hierarchical Equations of Motion,<sup>20-22</sup> in addition to approximate methods like Redfield theory,<sup>23,24</sup> Fewest Switches Surface Hopping and other mixed quantum-classical dynamics methods,<sup>25-31</sup> and Semiclassical theories.<sup>32-39</sup> Unfortunately, the majority of these approaches are not suitable for large scale system simulations, with a notable exception being systems that can be modeled by spin-boson Hamiltonians where transitions between electronic states are mediated by coupling to a nuclear bath. Approximate imaginary-time path integral methods like Centroid Molecular Dynamics (CMD)<sup>40,41</sup> and Ring Polymer Molecular Dynamics (RPMD)<sup>42</sup> show great promise in moving beyond the spin-boson models to the more complex bilinear coupling Hamiltonian models and even atomistic simulations.<sup>43-58</sup> Both CMD and RPMD conserve the quantum Boltzmann distribution and capture nuclear quantum effects like tunneling using an ensemble of classical trajectories in an extended phase space, making them efficient for the simulation of systems with many degrees of freedom. Nonadiabatic extensions of CMD have been explored in the context of the spin-boson model,<sup>53</sup> while RPMD has been used for atomistic simulations of nonadiabatic electron transfer and proton-coupled electron transfer<sup>50,52</sup> However, it has been shown that RPMD cannot capture state-to-state dynamics when working with a two-level or, in general,  $K$ -level system Hamiltonian.<sup>50</sup> This limitation has motivated the development of several multi-state imaginary-time path integral based methods including mean-field (MF)-RPMD,<sup>59-61</sup> nonadiabatic RPMD,<sup>62</sup> kinetically constrained (KC)-RPMD,<sup>63-65</sup> coherent-state RPMD,<sup>66</sup> and mapping-variable (MV)-RPMD.<sup>67-70</sup> Other approaches have also been developed that combine RPMD with *ad hoc* nonadiabatic dynamics methods like surface hopping.<sup>71-74</sup>

Of these methods, only MV-RPMD and MF-RPMD retain the key RPMD feature of conserving the quantum Boltzmann distribution, and MF-RPMD is unique in that it does not introduce any explicit electronic variables, instead describing nuclear dynamics on an effective state-averaged potential energy surface. This makes MF-RPMD more approximate but significantly more efficient than MV-RPMD. Initial efforts to compute MF-RPMD rates used the nuclear centroid reaction coordinate and defined the dividing surface as configurations where the two electronic states were degenerate.<sup>60</sup> It was shown that the resulting rate expression significantly overestimated nonadiabatic reaction rates.<sup>60</sup> Subsequent work has established that this error can be attributed to the use of a dividing surface that does not require the formation of kinked ring polymer configurations (where at least one bead is in a different electronic state than the others), an essential intermediate step in state-to-state reactions.<sup>61,64</sup> Further, it has been established that this error can be mitigated by introducing a doubly-constrained dividing surface that requires formation of kinked configurations, however the resulting MF-RPMD rate expression proved challenging to implement.<sup>61</sup>

Here we introduce an improved reaction coordinate that tracks the difference in electronic state populations, and a modified reactive flux definition that accounts for the formation of kinked ring polymer configurations. We demonstrate that this new coordinate and reactive flux definition enable accurate calculations of nonadiabatic and adiabatic reaction rates for a series of bilinear coupling model systems, captures nonadiabatic electron transfer rates across a wide range of driving forces, and successfully incorporates nuclear quantum effects by reproducing FGR rates over a range of temperatures in models where the driving force places them in the Marcus normal regime. In the Marcus inverted regime, we show MF-RPMD reproduces Marcus theory rates rather than FGR rates. This failure to account for nuclear tunneling can be traced to the use of a Boltzmann weighted reaction coordinate that effectively limits the the ring polymer to sample only nuclear configurations where the two electronic states are degenerate.

# Methods

## Path Integrals for Multi-level Systems

For a general  $K$ -level system with  $d$  nuclear degrees of freedom, the diabatic Hamiltonian is

$$\hat{H} = \sum_{j=1}^d \frac{\hat{P}_j^2}{2M_j} + \sum_{n,m=1}^K |n\rangle V_{nm}(\hat{R}) \langle m|, \quad (1)$$

where  $\hat{R}$  and  $\hat{P}$  are  $d$ -dimensional nuclear position and momentum vector operators, respectively,  $M_j$  is the nuclear mass,  $\{|n\rangle\}$  is the set of diabatic states, and  $V_{nm}(\hat{R})$  is the diabatic potential energy operator. The quantum canonical partition function is obtained by evaluating the trace in the basis of nuclear positions and electronic states, and discretized via repeated insertion of  $N$  copies of identity in the form of completeness relations to obtain

$$\begin{aligned} Z &= \text{Tr}[e^{-\beta\hat{H}}] \\ &= \int d\{R_\alpha\} \sum_{\{n_\alpha\}=1}^K \prod_{\alpha=1}^N \langle R_\alpha, n_\alpha | e^{-\beta_N \hat{H}} | R_{\alpha+1}, n_{\alpha+1} \rangle, \end{aligned} \quad (2)$$

where  $\beta_N = 1/(Nk_B T)$ ,  $T$  is temperature,  $N$  is the number of imaginary time slices (or beads), and  $R_\alpha, n_\alpha$  refer to the nuclear position and electronic state, respectively, of the  $\alpha^{\text{th}}$  bead. In Eq. 2, the shorthand,  $\int d\{R_\alpha\} = \int dR_1 \int dR_2 \dots \int dR_N$  and  $\sum_{\{n_\alpha\}=1} = \sum_{n_1} \sum_{n_2} \dots \sum_{n_N}$ , is used to represent the multi-dimensional integral over nuclear coordinates and summation over electronic states. The matrix elements in Eq. 2 are evaluated using the Trotter (high temperature) approximation to obtain,<sup>75,76</sup>

$$Z \propto \lim_{N \rightarrow \infty} \int \{dR_\alpha\} e^{-\beta_N V_N(\{R_\alpha\})} \text{Tr}[\Gamma], \quad (3)$$

where

$$V_N = \sum_{j=1}^d \sum_{\alpha=1}^N \left[ \frac{M_j}{2\beta_N^2} (R_{j,\alpha} - R_{j,\alpha+1})^2 \right], \quad (4)$$

$$\Gamma = \prod_{\alpha=1}^N \mathbf{M}(R_{\alpha}), \quad (5)$$

and  $\mathbf{M}$  is the  $K \times K$ -dimensional matrix

$$M_{nm}(R_{\alpha}) = \begin{cases} e^{-\beta_N V_{nn}(R_{\alpha})} & n = m \\ -\beta_N V_{nm}(R_{\alpha}) e^{-\beta_N V_{nn}(R_{\alpha})}. & n \neq m \end{cases} \quad (6)$$

The trace in Eq. 3 can be moved into the exponential, and  $N$  normalized nuclear momentum gaussians can be introduced to express the canonical partition function as a phase space integral,

$$Z \propto \lim_{N \rightarrow \infty} \int \{dR_{\alpha}\} \int \{dP_{\alpha}\} e^{-\beta_N H_N(\{R_{\alpha}\}, \{P_{\alpha}\})}, \quad (7)$$

where the Mean-Field Ring Polymer Hamiltonian is

$$H_N = \sum_{j=1}^d \sum_{\alpha=1}^N \left[ \frac{M_j}{2\beta_N^2} (R_{j,\alpha} - R_{j,\alpha+1})^2 + \frac{P_{j,\alpha}^2}{2M_j} \right] - \frac{1}{\beta_N} \ln(\text{Tr}[\Gamma]). \quad (8)$$

In Eq. 8, the Hamiltonian is a function of nuclear phase space variables only, with an effective mean-field potential,  $V_{\text{MF}} = -\frac{1}{\beta_N} \ln(\text{Tr}[\Gamma])$ , obtained by tracing over all possible electronic state configurations for the ring polymer. During a state-to-state reaction, the contributions to the effective potential from ring polymer configurations where all the beads are in a single electronic state and configurations where the beads are in different electronic states will vary as the system moves from the reactant to product state as shown in Fig. 1.

## The MF-RPMD Approximation to Reaction Rates

The MF Hamiltonian in Eq. 8 can be used to generate molecular dynamics trajectories that sample equilibrium configurations of the  $K$ -level system at finite temperature as is done in standard Path Integral Molecular Dynamic simulations. MF-RPMD approximates the Kubo-transformed real-time quantum correlation function by sampling trajectory initial

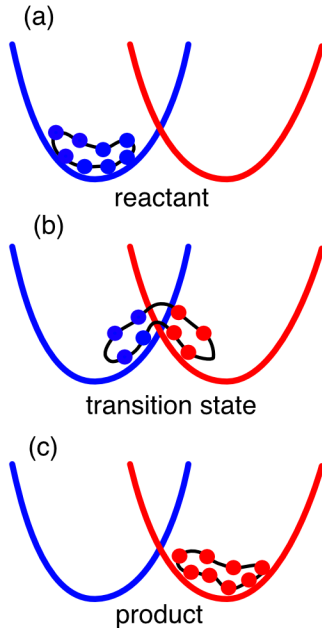


Figure 1: Cartoon showing the progress of a multi-level system reaction with state-space path integrals. In the reactant and product states, ring polymer configurations where all beads are in a single electronic state are the dominant contributions to the effective mean-field potential. At the transition state, when the system is moving from one state to the other, we expect to see a significant contribution from multi-electronic state or kinked ring polymer configurations.<sup>77</sup>

conditions from an exact quantum canonical ensemble and time-evolving them under the mean-field Hamiltonian. By construction, MF-RPMD trajectories preserve the quantum Boltzmann distribution.

The MF-RPMD approximation to the flux-side correlation function, in keeping with the RPMD approximation,<sup>78</sup> can be written as,

$$C_{\text{fs}}^{\text{MF}}(t) = \frac{\langle \delta(\xi_0 - \xi^\ddagger) \dot{\xi}_0 h(\xi_t - \xi^\ddagger) \rangle}{\langle h(\xi^\ddagger - \xi_0) \rangle}, \quad (9)$$

where  $\langle \dots \rangle$  indicates a canonical ensemble average. The reaction coordinate,  $\xi$ , in Eq. 9 is a function of the ring polymer nuclear configurations  $\{R\}$ , with  $\xi_0$  being its value at time  $t = 0$ ,  $\xi_t$  the value at any later time  $t$ , and  $\xi^\ddagger$  defines the dividing surface. For reactions involving transitions between electronic states, although there are no explicit electronic state

variables in the MF-RPMD Hamiltonian, previous work suggests that it is essential that the definition of the reactive flux properly accounts for the formation of ‘kinked’ ring polymer configurations as shown in Fig 1.<sup>61,63,77</sup> Unfortunately, for nonadiabatic processes, sampling the dividing surface  $\xi = \xi^\ddagger$  in Eq. 9 with the mean-field Hamiltonian yields an ensemble of ring polymer configurations where all beads are in a single electronic state rather than kinked configurations. The origin of this difficulty is well understood: the probability of kink formation is proportional to the square of the diabatic coupling, making this a rare event in the nonadiabatic regime where coupling values are very small. In the language of the mean-field effective potential,

$$\Gamma = \Gamma_1 + \Gamma_2 + \Gamma_k, \quad (10)$$

where  $\Gamma_i$ ,  $i = 1, 2$ , represent the potential contribution from configurations where all ring polymer beads are in the same electronic state,

$$\Gamma_i = \prod_{\alpha=1}^N [\mathbf{M}(R_\alpha) \mathcal{P}_i], \quad (11)$$

where  $\mathcal{P}_i$  is the projection operator matrix corresponding to the  $i^{\text{th}}$  electronic state, and the matrix elements of  $\mathbf{M}$  are defined in Eq. 6. The contribution to the effective potential from kinked ring polymer configurations,  $\Gamma_k$ , has a coupling-square dependence that ensures that it is *not* the dominant contribution to the  $\Gamma$  function at any nuclear configuration.

To sample *only* kinked configurations at the dividing surface, it is necessary to introduce an *ad hoc* modification to the dividing surface that re-weights the sampling,

$$\delta(\xi - \xi^\ddagger) \rightarrow \delta(\xi - \xi^\ddagger) \frac{\text{Tr} [\Gamma_k]}{\text{Tr} [\Gamma]}. \quad (12)$$

Using the modified dividing surface, the MF-RPMD rate can be expressed as,

$$k = \lim_{t \rightarrow t_{\text{plateau}}} \frac{\int d\{R_\alpha, P_\alpha\} e^{-\beta_N H_N^0} \text{Tr} [\Gamma_k] \delta(\xi_0 - \xi^\ddagger) \dot{\xi}_0 h(\xi_t - \xi^\ddagger)}{\int d\{R_\alpha, P_\alpha\} e^{-\beta_N H_N^0} \text{Tr} [\Gamma_1]}, \quad (13)$$

where  $H_N^0$  is the free ring polymer Hamiltonian that includes only the harmonic spring term and the kinetic energy terms of Eq. 8 and the presence of  $\Gamma_k$  ensures that the effective potential samples only kinked configurations. The time-evolved reaction coordinate,  $\xi_t$ , is obtained by integrating the classical equations of motion due to the MF-RPMD Hamiltonian in Eq. 8. The denominator in Eq. 13 is the reactant partition function, and is calculated by sampling configurations projected onto the reactant (here, state 1).

We now introduce a new reaction coordinate, a bead-averaged population difference estimator that was previously employed in the context of MF-RP instanton calculations,<sup>59,79</sup> and is exact at equilibrium,

$$\Delta P = \frac{1}{N} \sum_{\alpha=1}^N \frac{e^{-\beta_N V_{22}(R_\alpha)} - e^{-\beta_N V_{11}(R_\alpha)}}{e^{-\beta_N V_{11}(R_\alpha)} + e^{-\beta_N V_{22}(R_\alpha)}}. \quad (14)$$

This coordinate takes negative values in the reactant region, positive values in the product region, and is zero at the dividing surface. The corresponding MF-RPMD rate expression is then,

$$k = \lim_{t \rightarrow t_{\text{plateau}}} \frac{\int d\{R_\alpha, P_\alpha\} e^{-\beta_N H_N^0} \text{Tr} [\Gamma_k] \delta(\Delta P_0) \Delta \dot{P}_0 h(\Delta P_t)}{\int d\{R_\alpha, P_\alpha\} e^{-\beta_N H_N^0} \text{Tr} [\Gamma_1]}, \quad (15)$$

The population coordinate and dividing surface introduced here are significantly different from the coordinate previously introduced by one of us.<sup>61</sup> In that work, the dividing surface was defined as nuclear configurations where half the ring polymer beads were in one state and the other half were in a different state. In addition, the reaction coordinate measured

population differences but with the so-called Boltzmann estimator,<sup>70</sup> is given by

$$\chi = \frac{\text{Tr} \left[ \prod_{\alpha=1}^N \mathbf{M}(R_{\alpha}) |2\rangle \langle 2| \right] - \text{Tr} \left[ \prod_{\alpha=1}^N \mathbf{M}(R_{\alpha}) |1\rangle \langle 1| \right]}{\text{Tr} \left[ \prod_{\alpha=1}^N \mathbf{M}(R_{\alpha}) |2\rangle \langle 2| \right] + \text{Tr} \left[ \prod_{\alpha=1}^N \mathbf{M}(R_{\alpha}) |1\rangle \langle 1| \right]} \quad (16)$$

While both population estimators are exact at equilibrium in the mean-field path integral framework, the coordinate used here,  $\Delta P$  as defined Eq. 14, has been previously used to track changes in electronic state populations along the mean-field ring polymer instantons.<sup>59,79</sup> There are two significant advantages to the present  $\Delta P$  coordinate. First, this coordinate is a bead-average population difference coordinate ensuring that the time zero correlation function correctly corresponds to a Kubo-transform real-time thermal correlation function. Second,  $\Delta P$  can be easily computed in large scale simulations where the donor and acceptor state potentials are known ( $V_{11}$  and  $V_{22}$ ), and does not require the matrix multiplication steps necessary to construct the  $\chi$  coordinate. As a final point of comparison, we note that the velocity corresponding to  $\chi$  was computed numerically using finite difference,<sup>61</sup> whereas the analytic time derivative of  $\Delta P$  is easily computed.

Our new rate expression defined in Eq. (15) has some parallels with the rate formalism of KC-RPMD.<sup>64</sup> Both methods emphasize the formation of kinked RP configurations to accurately described nonadiabatic reaction rates, but differ in the details. In KC-RPMD, the reaction coordinate is defined by an auxiliary dynamical variable that reports on the formation of kink-pairs; the introduction of this variable results in a modified Boltzmann distribution that the KC-RPMD Hamiltonian conserves. The MF-RPMD rate presented here does not introduce any additional dynamical variables, with our reaction coordinate depending only on the RP bead positions and the diabatic potential energy surfaces. Further, in KC-RPMD, the restriction that nonadiabatic transitions should occur at configurations where the diabatic states are near-degenerate is enforced by the use of a penalty function on kinked configurations in the effective potential in the form of a Gaussian of the scaled energy difference of the diabatic surfaces. In the present work, we ensure kink formation near the

diabatic state crossing through our modified dividing surface.

## Reference Rate Theories

We compare nonadiabatic MF-RPMD rates computed here against Marcus theory and FGR rates. The Marcus theory rate for a nonadiabatic process with a classical solvent is,<sup>1</sup>

$$k_{\text{MT}} = \frac{2\pi}{\hbar} |V_{nm}|^2 \sqrt{\frac{\beta}{4\pi\lambda}} e^{-\beta(\lambda-\varepsilon)^2/4\lambda}, \quad (17)$$

where  $\lambda$  is the reorganization energy,  $\varepsilon$  is the driving force, and  $V_{nm}$  is the diabatic coupling between the reactant and product electronic states.

FGR rate theory for a nonadiabatic reaction using the flux correlation formalism is,<sup>80</sup>

$$k_{\text{FGR}} = \frac{1}{Z_0} \frac{\Delta^2}{\hbar^2} \int_{-\infty}^{\infty} dt C^\tau(t), \quad (18)$$

where

$$C^\tau(t) = \text{Tr} \left[ e^{i\hat{H}_0(t+i(\beta\hbar-\tau))/\hbar} e^{-i\hat{H}_1(t-i\tau)/\hbar} \right], \quad (19)$$

$Z_0 = \text{Tr} \left[ e^{-\beta\hat{H}_0} \right]$  is the reactant partition function.  $\hat{H}_0$  and  $\hat{H}_1$  are the Hamiltonians representing the reactant and product states respectively.  $\tau$  can be any real number as the rate is independent of its choice<sup>80</sup> but is, typically, chosen to be in the range  $[0, \beta\hbar]$ . For the bilinear coupling model Hamiltonians employed here, the FGR rate can be obtained analytically;<sup>81</sup> Details of this calculation are provided in the Supporting Information.

In the adiabatic limit, the electron transfer rate constant for a system with quantum solvent can be expressed using Kramers theory,<sup>82</sup>

$$k_{\text{KT}} = \left( \sqrt{1 + \left( \frac{\gamma}{2\omega_b} \right)^2} - \frac{\gamma}{2\omega_b} \right) \frac{\omega_s}{2\pi} e^{-\beta G_{\text{cl}}^\ddagger}, \quad (20)$$

where  $\omega_s$  is the frequency of the harmonic potential,  $\omega_b$  is the frequency at the barrier top,

$\gamma = \eta/M_s$ ,  $\eta$  is the strength of the coupling to a dissipative bath,  $M_s$  is the solvent mass, and  $G_{\text{cl}}^\ddagger$  is the free energy barrier computed for a classical solvent.

## Model Systems

We calculate rates for a series of bilinear vibronic coupling models of condensed phase electron transfer with potential

$$V(\hat{R}) = V_S(\hat{s}) + V_B(\hat{R}) \quad (21)$$

where the configuration vector  $\hat{R} = \{\hat{s}, \hat{Q}\}$  represents the solvent polarization coordinate,  $s$ , and the bath coordinates,  $Q$ . The diabatic potential energy matrix is

$$V_S(\hat{s}) = \begin{pmatrix} A\hat{s}^2 + B\hat{s} + \varepsilon & \Delta \\ \Delta & A\hat{s}^2 - B\hat{s} \end{pmatrix}, \quad (22)$$

where  $\varepsilon$  is the driving force of the reaction and  $\Delta$  is the constant diabatic coupling. The solvent coordinate is linearly coupled to a thermal bath of  $f$  harmonic oscillators,

$$V_B(\hat{R}) = \sum_{j=1}^f \left[ \frac{1}{2} M_B \omega_j^2 \left( \hat{Q}_j - \frac{c_j \hat{s}}{M_B \omega_j^2} \right)^2 \right] \quad (23)$$

where  $M_B$  is the bath mass. The bath is described by an Ohmic spectral density

$$J(\omega) = \eta \omega e^{-\frac{\omega}{\omega_c}} \quad (24)$$

where  $\omega_c$  is the cutoff frequency and  $\eta$  is the dimensionless friction coefficient. The spectral density is discretized into  $f$  oscillators<sup>43</sup>

$$\omega_j = -\omega_c \ln \left( \frac{j - 0.5}{f} \right), \quad (25)$$

with coupling strengths

$$c_j = \omega_j \left( \frac{2\eta M_B \omega_c}{f\pi} \right)^{1/2}. \quad (26)$$

The parameters for this model are shown in Table 1.

**Table 1: Linear vibronic coupling model parameters in atomic units unless otherwise indicated.**

Parameters	Value
$A$	$4.772 \times 10^{-3}$
$B$	$2.288 \times 10^{-2}$
$\varepsilon$	0.0 – 0.2366
$\Delta$	$6.69 \times 10^{-7}$ - $1.20 \times 10^{-2}$
$M_S$	1836.0
$M_B$	1836.0
$f$	12
$\omega_c$	$2.28 \times 10^{-3}$
$\eta/M_B\omega_c$	1.0
$T$	150 - 300 K

We further investigate a set of spin-boson models previously benchmarked using Hierarchy Equations of Motion (HEOM) against RPMD and Wolynes theory.<sup>74</sup> These models allow us to investigate the performance of MF-RPMD in the overdamped and underdamped regimes for both high frequency (B2 and B4) and low frequency (B1 and B3) systems. Parameters for all four models are shown in Table 2, with the shared parameters reported in Table 3.

**Table 2: Parameters (in atomic units) used for the diabatic potential in Eq. (21) that defines the spin-boson models B1-B4.**

Parameters	B1	B2	B3	B4
$A$	0.125	8	0.125	8
$B$	2.739	21.909	2.739	21.909
$\eta/M_B\omega_c$	32	32	1	1
$\omega_c$	0.5	4	0.5	4

**Table 3: Shared parameters for the spin-boson models B1-B4 in atomic units.**

Parameters	Value
$\varepsilon$	15
$\Delta$	0.1585, 1, 2.5119
$M_S$	1.0
$M_B$	1.0
$f$	12
$\beta$	1

### Simulation Details

The numerator of the rate in Eq. 13 requires constrained sampling to the dividing surface while the denominator requires sampling the reactant region. We ensure sampling of all relevant configuration space using a windowing approach that introduces identity in the form of an integral over all solvent ring polymer centroid configurations. The resulting rate expression is

$$k = \lim_{t \rightarrow t_{\text{plateau}}} \frac{\int ds' \langle \text{Tr}[\Gamma_k] \delta(\Delta P_0) \Delta P_0 h(\Delta P_t) \rangle_w}{\int ds' \langle \text{Tr}[\Gamma_1] \rangle_w} \quad (27)$$

where  $\langle \dots \rangle_w$  is used to indicate a phase space ensemble average over the nuclear bead configurations obtained by importance sampling from the constrained distribution

$$w = e^{-\beta_N H_N^0(\{R_\alpha, P_\alpha\}) - k_s(\bar{s} - s')^2}, \quad (28)$$

where  $\bar{s}$  is the solvent ring polymer centroid. The integral in Eq. 27 is evaluated performed by ensemble averaging for a series of windows centered at different values of  $s'$ , and then using the trapezoid rule. A standard Metropolis algorithm is used to sample free ring polymer configurations from  $e^{-\beta_N H_N^0(\{R_\alpha, P_\alpha\})}$  subject to a harmonic constraint with force constant  $k = 1000$  a.u. on the centroid. We use 150 evenly spaced windows over a range of  $s'$  values. The initial value of  $s'$  for each model is given in Table S1 in the Supporting Information.

All MF-RPMD simulations presented here are converged with respect to bead number, as reported in the results section, convergence numbers range from  $N = 16 - 32$ . Ini-

tial conditions are sampled from  $5 \times 10^4$  decorrelated Monte Carlo steps for each window, and time-evolved under the mean-field Hamiltonian in Eq. 8 using a fourth-order Adams-Bashforth-Moulton predictor-corrector integrator with a time step of 0.05 a.u. for models I-VIII and 0.0005 a.u. for models B1-4. The flux-side correlation function plateau in time is achieved between 500 a.u. and 3000 a.u. for models I-VIII and between 5 a.u. to 300 a.u. for the B1-4 models.

The delta function at time zero in Eq. 27 is approximated with the Gaussian,

$$\delta(\Delta P) \approx \frac{1}{\sigma\sqrt{2\pi}} e^{-\frac{1}{2}\left(\frac{\Delta P}{\sigma}\right)^2}, \quad (29)$$

where  $\sigma$  is treated a parameter controlling the width of the Gaussian. Results reported here employ  $\sigma = 0.01 - 0.001$ ; values that are sufficiently small to mimic a delta function, but sufficiently large to ensure meaningful statistics in terms of number of trajectories and number of windows contributing to the overall rate integral. We ensure that the rates reported are consistent across at least two smaller  $\sigma$  values for each model. The analytical gradient of the population difference coordinate is used to obtain the initial velocity along the reaction coordinate in Eq. 9.

The flux-side correlation function in Eq. 13 assumes that the velocity is ‘positive’ when the system is moving from reactant to product. In the inverted regime, the analytic time-derivative of the population difference coordinate can be negative for trajectories starting on the reactant side of the minimum, and this can yield a reaction rate that is negative. We correct this by including a sign function that changes the sign of an individual bead’s contribution to ensure that the bead-average velocity has a positive sign when the trajectory is moving towards product formation,

$$\Delta \dot{P} = \frac{1}{N} \sum_{\alpha} \Delta \dot{P}_{\alpha} \quad (30)$$

$$\Delta \dot{P}_{\alpha} = -\text{sgn}(\Delta P_{\alpha}) \quad (31)$$

# Results and Discussion

We start with a study of MF-RPMD rates for nonadiabatic reactions with different driving forces at temperature  $T = 300$  K and with the diabatic coupling  $\Delta = 6.69 \times 10^{-7}$ . As shown in Fig. 2, we find MF-RPMD rates in quantitative agreement with FGR rates for Models I-IV that are in the Marcus normal regime. The results shown in the figure are also tabulated in Table 4, with all results calculated using  $\sigma = 0.01$  in Eq. 29. Note that we also calculate MF-RPMD rates using a centroid coordinate for normal regime models I, II, and IV, but do not plot the results since they are visually indistinguishable from the population coordinate results shown here. The rate expression with the centroid coordinate and the resulting MF-RPMD rates are provided in the SI.

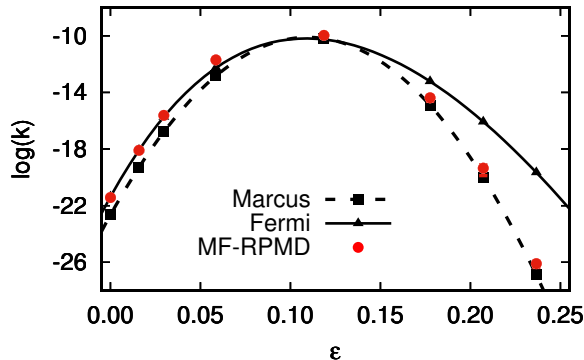


Figure 2: Nonadiabatic rates for bilinear coupling models I-VIII. MF-RPMD rates with are shown with red circles. FGR rates (triangles and solid line) and the Marcus theory rates (squares and dashed line) are also shown.

In the inverted regime, for models V-VIII, the MF-RPMD rate is in agreement with the Marcus Theory rate, despite the fact that MF-RPMD quantizes the solvent coordinate. We find that our definition of the dividing surface at  $\Delta P = 0$  is responsible for this discrepancy. As the population of each state is defined using the Boltzmann weight of that state, the state with the lower energy will have a higher population. In the normal regime,  $\Delta P = 0$

can be achieved by tunneling configurations where some beads are to the left of the crossing with  $\Delta P < 0$  and some are to the right with  $\Delta P > 0$  resulting in a bead-average value of zero. In the inverted regime, this remains true, however, tunneling configurations where all beads are to the right of the crossing fail to meet the  $\Delta P = 0$  criterion as shown in the cartoon Fig. 3. This result highlights one of the limitations of using MF-RPMD: the lack of an explicit electronic variable means that constraining to kinked configurations places potentially unphysical constraints on the nuclear configurations. In contrast, although KC-RPMD also employs a kink-constrained dividing surface, the constraint applies only to the auxiliary electronic variable introduced in that framework, allowing the method to capture nuclear tunneling in the Marcus inverted regime.

One of the strengths of MF-RPMD is the ability to accurately compute both adiabatic and nonadiabatic reaction rates within a single framework. We demonstrate this using model I, a normal regime model at  $T = 300$  K, and we plot the results calculated using  $\sigma = 0.01$  in Eq. 29 against the Marcus and FGR rates in Fig. 4, and tabulate them in Table 5. We find that MF-RPMD rates move seamlessly from good agreement with FGR rates in the nonadiabatic cases to good agreement with Kramer’s theory rates in the adiabatic regime.

Further, we examine the effect of temperature on the rate constant. For this we choose a model in the normal regime, model II, in the weak coupling limit  $\Delta = 6.69 \times 10^{-7}$ . For these simulations we use a value of  $\sigma = 0.001$  in Eq. 29. The results are shown in Fig. 5 and

**Table 4: Nonadiabatic reaction rates for models I-VIII**

Model	$\varepsilon$	$\log(k_{\text{MF}})$	$\log(k_{\text{FGR}})$	$\log(k_{\text{MT}})$
I	0.00	-21.42	-21.37	-22.65
II	0.0158	-18.09	-18.08	-19.30
III	0.0296	-15.60	-15.73	-16.79
IV	0.0586	-11.70	-12.26	-12.83
V	0.1186	-9.97	-10.26	-10.19
VI	0.1776	-14.38	-13.22	-14.91
VII	0.2071	-19.35	-16.07	-19.99
VIII	0.2366	-26.10	-19.65	-26.89

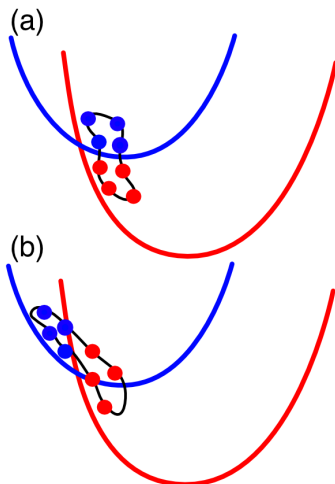


Figure 3: Cartoon of RP configurations in the inverted regime showing kinked configurations where some beads are in the reactant state and others are in the product state. Although configurations in (a) are quantum mechanically valid and necessary to capture solvent tunneling, in our MF-RPMD simulation they correspond to  $\Delta P \neq 0$ . Configurations in (b) do obey the  $\Delta P = 0$  criterion. For this reason, the MF-RPMD rates reported here fail to reproduce FGR rates in the inverted regime, instead yielding Marcus theory rates.

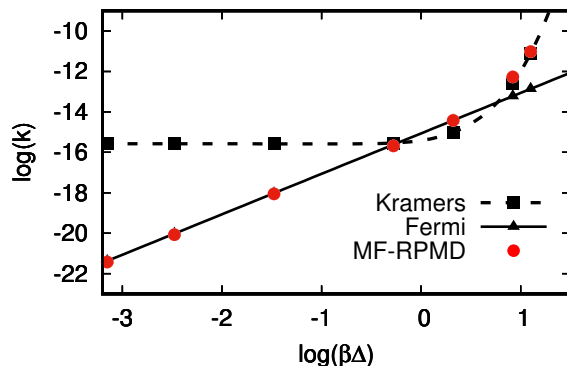


Figure 4: Reactions rates for model I with coupling strength modified to tune the system with varying coupling. MF-RPMD rates with the new population dividing surface are shown as red circles and the error bars are within the symbol size. The FGR rate (triangles and solid line) and the Kramers theory rate (squares and dashed line) are also shown

tabulated in Table 6. Consistent with our other results in the normal regime, we achieve quantitative agreement with the rates from Fermi's golden rule. As expected, we do have to increase the number of beads from 16 to 24 to get converged results at lower temperatures. At very high temperatures, as suggested by earlier studies,<sup>83</sup> the present rate expression is expected to perform poorly given the *ad hoc* nature of the dividing surface introduced.

**Table 5: Reaction rates for model I with variable coupling**

$\Delta$	$N$	$\log(k_{\text{MF}})$	$\log(k_{\text{FGR}})$	$\log(k_{\text{KT}})$
$6.69 \times 10^{-7}$	16	-21.42	-21.37	-15.57
$3.16 \times 10^{-6}$	16	-20.07	-20.02	-15.58
$3.16 \times 10^{-5}$	16	-18.06	-18.02	-15.58
$5.01 \times 10^{-4}$	32	-15.68	-15.62	-15.54
$2.00 \times 10^{-3}$	32	-14.42	-14.42	-15.02
$7.94 \times 10^{-3}$	32	-12.27	-13.22	-12.60
$1.20 \times 10^{-2}$	32	-11.02	-12.86	-11.11

Indeed, we find this is the case at  $T = 5000K$  comparing the 8-bead MF-RPMD rate (1-bead is the zero-coupling limit) against the corresponding FGR rate, we find the rate differs by almost an order of magnitude,  $k_{\text{FGR}} = 5.36 \times 10^{-12}$  a.u. and  $k_{\text{MF}} = 1.56 \times 10^{-13}$  a.u.

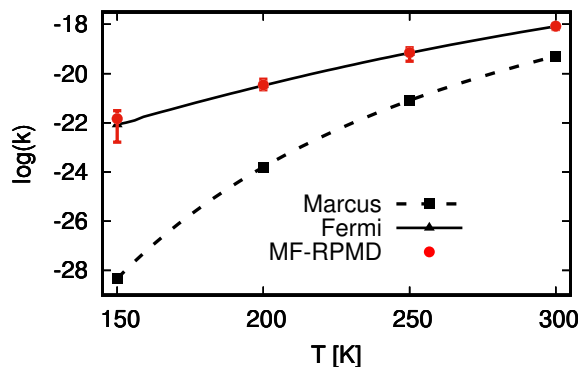


Figure 5: ET rates as function of temperature for model II with  $\varepsilon = 0.0158$ . MF-RPMD rates with the new population dividing surface are shown as red circles. The Fermi's golden rule (triangles and solid line) and the Kramers theory (squares and dashed line) rates are also shown

Finally, we present the MF-RPMD rates for models B1-B4. The results are shown in Fig. 6 and tabulated in Table 7. Overall, we find relatively good agreement when against FGR and Kramer's rate theory results as the systems move from the nonadiabatic to the adiabatic regime. The most significant error is for the case of low frequency and strong system-bath coupling where we find the nonadiabatic MF-RPMD rates significantly underestimate the FGR rates. This appears to be in keeping with the limitations of the current rate expression that does not correctly capture classical-limit behavior.

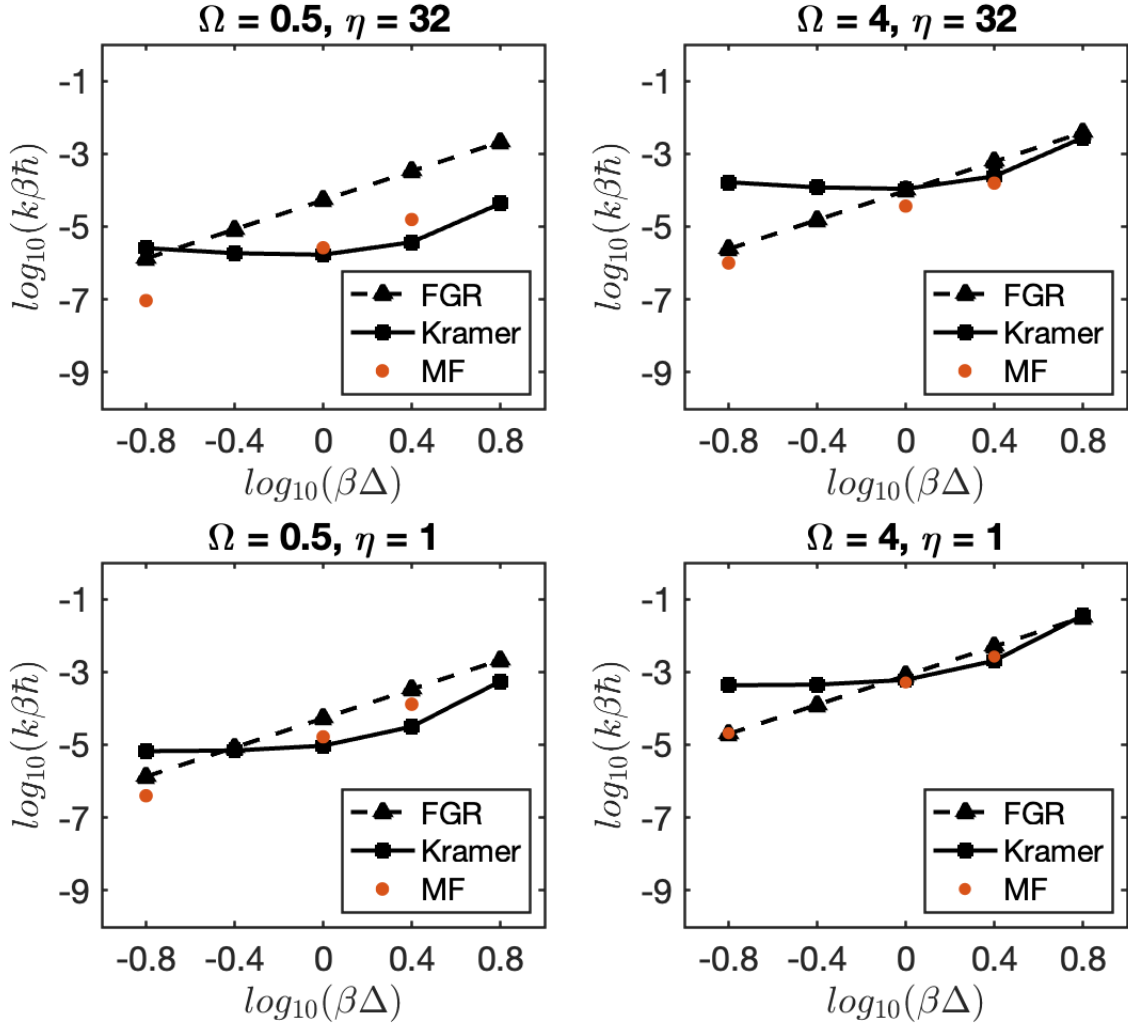


Figure 6: MF-RPMD reaction rates for the spin-boson models B1-B4 as a function of coupling strength. The MF-RPMD rates (red circles) are compared against with The Fermi's golden rule (triangles and solid line) and the Kramers theory (squares and dashed line)

Table 6: MF-RPMD rates for the linear vibronic coupling model with varying temperature

T (K)	$N$	$\log(k_{\text{MF}})$	$\log(k_{\text{FGR}})$	$\log(k_{\text{MT}})$
150	24	-21.84	-22.07	-28.33
200	24	-20.46	-20.48	-23.80
250	16	-19.15	-19.16	-21.09
300	16	-18.07	-18.08	-19.30

**Table 7: MF-RPMD rates for the spin-boson models B1-B4**

Model	$\log(\beta\Delta)$	$\log(k_{\text{MF}})$	$\log(k_{\text{FGR}})$	$\log(k_{\text{Kramer}})$
B1	-0.8	-7.03	-5.88	-5.59
	0	-5.58	-4.28	-5.77
	0.4	-4.80	-3.48	-5.43
B2	-0.8	-6.00	-5.62	-3.78
	0	-4.44	-4.02	-3.96
	0.4	-3.81	-3.22	-3.62
B3	-0.8	-6.40	-5.87	-5.18
	0	-4.78	-4.27	-5.03
	0.4	-3.89	-3.47	-4.50
B4	-0.8	-4.68	-4.70	-3.37
	0	-3.29	-3.10	-3.22
	0.4	-2.58	-2.30	-2.70

## Conclusions

We introduce a new population difference reaction coordinate and a kink-constrained dividing surface for the calculation of rates using MF-RPMD. This new rate formulation represents a simplification of the previously introduced MF-RPMD rate expression for multi-level systems with an implementation that is designed to enable atomistic system simulations. We have shown that the MF-RPMD rate expression introduced here is accurate over a wide range of electronic coupling strengths, captures nonadiabatic rates accurately over a range of driving forces, and is able to capture nuclear tunneling effects at low temperatures.

Future directions include identifying modifications to the current protocol to enable capturing tunneling in the inverted regime, and addressing the inaccuracies in rate as we approach classical-limit behavior. While the current implementation is scalable to atomistic simulations where reactant and product state are defined in the diabatic framework using methods like the multi-state empirical valence band model,<sup>84</sup> we are also investigating working with the adiabatic rather than diabatic states to enable on-the-fly simulations, an attractive direction given that the MF-RPMD Hamiltonian is agnostic to the choice of electronic state representation.

## Acknowledgements

N.A., B.A.J., and N. L. acknowledge support from the U.S. Department of Energy, Office of Basic Energy Sciences, Division of Chemical Sciences, Geosciences and Biosciences under Award DE-FG02-12ER16362 (Nanoporous Materials Genome: Methods and Software to Optimize Gas Storage, Separations, and Catalysis). B.A.J. acknowledges current support by the DOE Office of Science, Office of Basic Energy Sciences, Division of Chemical Sciences, Geosciences, and Biosciences, Condensed Phase and Interfacial Molecular Science program. S.B. acknowledges support from Cornell University, Department of Chemistry and Chemical Biology.

## Supporting Information Available

Additional simulations details for MF-RPMD implementation and details of the analytic expression for calculating the FGR rate for bilinear coupling model Hamiltonians are provided in the supporting information.

## References

- (1) Marcus, R. A.; Sutin, N. Electron Transfers in Chemistry and Biology. *Biochim. Biophys. Acta* **1985**, *811*, 265–322.
- (2) Gray, H. B.; Winkler, J. R. ELECTRON TRANSFER IN PROTEINS. *Annu. Rev. Biochem.* **1996**, *65*, 537–561.
- (3) Skourtis, S. S.; Waldeck, D. H.; Beratan, D. N. Fluctuations in Biological and Bioinspired Electron-Transfer Reactions. *Annu. Rev. Phys. Chem.* **2010**, *61*, 461–485.
- (4) Azzouzi, M.; Yan, J.; Kirchartz, T.; Liu, K.; Wang, J.; Wu, H.; Nelson, J. Nonradiative

- Energy Losses in Bulk-Heterojunction Organic Photovoltaics. *Phys. Rev. X* **2018**, *8*, 031055.
- (5) Yarkony, D. R. Nonadiabatic Quantum Chemistry: Past, Present, and Future. *Chem. Rev.* **2012**, *112*, 481–498.
- (6) Hammes-Schiffer, S.; Soudackov, A. V. Proton-Coupled Electron Transfer in Solution, Proteins, and Electrochemistry. *J. Phys. Chem. B* **2008**, *112*, 14108–14123.
- (7) Marcus, R. A. On the Theory of Oxidation-Reduction Reactions Involving Electron Transfer. I. *J. Chem. Phys.* **1956**, *24*, 966–978.
- (8) Wolynes, P. G. Imaginary Time Path Integral Monte Carlo Route to Rate Coefficients for Nonadiabatic Barrier Crossing. *J. Chem. Phys.* **1987**, *87*, 6559–6561.
- (9) Lawrence, J. E.; Manolopoulos, D. E. Analytic Continuation of Wolynes Theory into the Marcus Inverted Regime. *J. Chem. Phys.* **2018**, *148*, 102313.
- (10) Fang, W.; Thapa, M. J.; Richardson, J. O. Nonadiabatic Quantum Transition-State Theory in the Golden-Rule Limit. II. Overcoming the Pitfalls of the Saddle-Point and Semiclassical Approximations. *J. Chem. Phys.* **2019**, *151*, 214101.
- (11) Fang, W.; Zarotiadis, R. A.; Richardson, J. O. Revisiting Nuclear Tunnelling in the Aqueous Ferrous–Ferric Electron Transfer. *Phys. Chem. Chem. Phys.* **2020**, *22*, 10687–10698.
- (12) Lawrence, J. E.; Manolopoulos, D. E. An Improved Path-Integral Method for Golden-Rule Rates. *J. Chem. Phys.* **2020**, *153*, 154113.
- (13) Lawrence, J. E.; Manolopoulos, D. E. Confirming the Role of Nuclear Tunneling in Aqueous Ferrous–Ferric Electron Transfer. *J. Chem. Phys.* **2020**, *153*, 154114.
- (14) Lawrence, J. E.; Fletcher, T.; Lindoy, L. P.; Manolopoulos, D. E. On the Calculation of Quantum Mechanical Electron Transfer Rates. *J. Chem. Phys.* **2019**, *151*, 114119.

- (15) Beck, M. H.; Jäckle, A.; Worth, G. A.; Meyer, H. D. The Multiconfiguration Time-Dependent Hartree (MCTDH) Method: A Highly Efficient Algorithm for Propagating Wavepackets. *Physics Reports* **2000**, *324*, 1–105.
- (16) Han, S.; Schröder, M.; Gatti, F.; Meyer, H.-D.; Lauvergnat, D.; Yarkony, D. R.; Guo, H. Representation of Diabatic Potential Energy Matrices for Multiconfiguration Time-Dependent Hartree Treatments of High-Dimensional Nonadiabatic Photodissociation Dynamics. *J. Chem. Theory Comput.* **2022**, *18*, 4627–4638.
- (17) Makri, N. Quantum Dissipative Dynamics: A Numerically Exact Methodology. *J. Phys. Chem. A* **1998**, *102*, 4414–4427.
- (18) Chatterjee, S.; Makri, N. Real-Time Path Integral Methods, Quantum Master Equations, and Classical vs Quantum Memory. *J. Phys. Chem. B* **2019**, *123*, 10470–10482.
- (19) Makri, N. Small Matrix Path Integral for System-Bath Dynamics. *J. Chem. Theory Comput.* **2020**, *16*, 4038–4049.
- (20) Tanimura, Y.; Kubo, R. Time Evolution of a Quantum System in Contact with a Nearly Gaussian-Markoffian Noise Bath. *J. Phys. Soc. Jpn.* **1989**, *58*, 101–114.
- (21) Tanimura, Y.; Wolynes, P. G. Quantum and Classical Fokker-Planck Equations for a Gaussian-Markovian Noise Bath. *Phys. Rev. A* **1991**, *43*, 4131–4142.
- (22) Xing, T.; Li, T.; Liu, Y.; Shi, Q. Mixed Quantum Classical Reaction Rates Based on the Phase Space Formulation of the Hierarchical Equations of Motion. *Chinese Journal of Chemical Physics* **2022**, *35*, 727–737.
- (23) Redfield, A. G. On the Theory of Relaxation Processes. *IBM J. Res. Dev.* **1957**, *1*, 19–31.
- (24) Kimura, A. Time-Dependent Renormalized Redfield Theory. *Chemical Physics Letters* **2016**, *645*, 123–126.

- (25) Tully, J. C. Molecular Dynamics with Electronic Transitions. *J. Chem. Phys.* **1990**, *93*, 1061–1071.
- (26) Kapral, R. Progress in the Theory of Mixed Quantum-Classical Dynamics. *Annu. Rev. Phys. Chem.* **2006**, *57*, 129–157.
- (27) Jain, A.; Subotnik, J. E. Surface Hopping, Transition State Theory, and Decoherence. II. Thermal Rate Constants and Detailed Balance. *J. Chem. Phys.* **2015**, *143*, 134107.
- (28) Crespo-Otero, R.; Barbatti, M. Recent Advances and Perspectives on Nonadiabatic Mixed Quantum Classical Dynamics. *Chem. Rev.* **2018**, *118*, 7026–7068.
- (29) Miller, W. H.; Cotton, S. J. Classical Molecular Dynamics Simulation of Electronically Non-Adiabatic Processes. *Faraday Discuss.* **2016**, *195*, 9–30.
- (30) Cotton, S. J.; Miller, W. H. Symmetrical Windowing for Quantum States in Quasi-Classical Trajectory Simulations. *J. Phys. Chem. A* **2013**, *117*, 7190–7194.
- (31) Warburton, R. E.; Soudackov, A. V.; Hammes-Schiffer, S. Theoretical Modeling of Electrochemical Proton-Coupled Electron Transfer. *Chem. Rev.* **2022**, *122*, 10599–10650.
- (32) Cao, J.; Voth, G. A. A Unified Framework for Quantum Activated Rate Processes. II. The Nonadiabatic Limit. *J. Chem. Phys.* **1997**, *106*, 1769–1779.
- (33) Cao, J.; Minichino, C.; Voth, G. A. The Computation of Electron Transfer Rates: The Nonadiabatic Instanton Solution. *J. Chem. Phys.* **1995**, *103*, 1391–1399.
- (34) Richardson, J. O.; Bauer, R.; Thoss, M. Semiclassical Green’s Functions and an Instanton Formulation of Electron-Transfer Rates in the Nonadiabatic Limit. *J. Chem. Phys.* **2015**, *143*, 134115.
- (35) Richardson, J. O. Ring-Polymer Instanton Theory of Electron Transfer in the Nonadiabatic Limit. *J. Chem. Phys.* **2015**, *143*, 134116.

- (36) Lee, M. K.; Huo, P.; Coker, D. F. Semiclassical Path Integral Dynamics: Photosynthetic Energy Transfer with Realistic Environment Interactions. *Annu. Rev. Phys. Chem.* **2016**, *67*, 639–668.
- (37) Ananth, N.; Venkataraman, C.; Miller, W. H. Semiclassical Description of Electronically Nonadiabatic Dynamics via the Initial Value Representation. *J. Chem. Phys.* **2007**, *127*, 084114.
- (38) Church, M. S.; Hele, T. J. H.; Ezra, G. S.; Ananth, N. Nonadiabatic Semiclassical Dynamics in the Mixed Quantum-Classical Initial Value Representation. *J. Chem. Phys.* **2018**, *148*, 102326.
- (39) Liu, J.; He, X.; Wu, B. Unified Formulation of Phase Space Mapping Approaches for Nonadiabatic Quantum Dynamics. *Acc. Chem. Res.* **2021**, *54*, 4215–4228.
- (40) Cao, J.; Voth, G. A. The Formulation of Quantum Statistical Mechanics Based on the Feynman Path Centroid Density. II. Dynamical Properties. *J. Chem. Phys.* **1994**, *100*, 5106–5117.
- (41) Jang, S.; Voth, G. A. A Derivation of Centroid Molecular Dynamics and Other Approximate Time Evolution Methods for Path Integral Centroid Variables. *J. Chem. Phys.* **1999**, *111*, 2371–2384.
- (42) Craig, I. R.; Manolopoulos, D. E. Quantum Statistics and Classical Mechanics: Real Time Correlation Functions from Ring Polymer Molecular Dynamics. *J. Chem. Phys.* **2004**, *121*, 3368–3373.
- (43) Craig, I. R.; Manolopoulos, D. E. Chemical Reaction Rates from Ring Polymer Molecular Dynamics. *J. Chem. Phys.* **2005**, *122*, 084106.
- (44) Lawrence, J. E.; Manolopoulos, D. E. Path Integral Methods for Reaction Rates in Complex Systems. *Faraday Discuss.* **2020**, *221*, 9–29.

- (45) Novikov, I. S.; Suleimanov, Y. V.; Shapeev, A. V. Automated Calculation of Thermal Rate Coefficients Using Ring Polymer Molecular Dynamics and Machine-Learning Interatomic Potentials with Active Learning. *Phys. Chem. Chem. Phys.* **2018**, *20*, 29503–29512.
- (46) Hele, T. J. H.; Althorpe, S. C. Derivation of a True ( $t \rightarrow 0_+$ ) Quantum Transition-State Theory. I. Uniqueness and Equivalence to Ring-Polymer Molecular Dynamics Transition-State-Theory. *J. Chem. Phys.* **2013**, *138*, 084108.
- (47) Althorpe, S. C.; Hele, T. J. H. Derivation of a True ( $t \rightarrow 0_+$ ) Quantum Transition-State Theory. II. Recovery of the Exact Quantum Rate in the Absence of Recrossing. *J. Chem. Phys.* **2013**, *139*, 084115.
- (48) Hele, T. J. H.; Althorpe, S. C. An Alternative Derivation of Ring-Polymer Molecular Dynamics Transition-State Theory. *J. Chem. Phys.* **2016**, *144*, 174107.
- (49) Habershon, S.; Manolopoulos, D. E.; Markland, T. E.; Miller, T. F. Ring-Polymer Molecular Dynamics: Quantum Effects in Chemical Dynamics from Classical Trajectories in an Extended Phase Space. *Annu. Rev. Phys. Chem.* **2013**, *64*, 387–413.
- (50) Menzeleev, A. R.; Ananth, N.; Miller, T. F. Direct Simulation of Electron Transfer Using Ring Polymer Molecular Dynamics: Comparison with Semiclassical Instanton Theory and Exact Quantum Methods. *J. Chem. Phys.* **2011**, *135*, 074106.
- (51) Kenion, R. L.; Ananth, N. Direct Simulation of Electron Transfer in the Cobalt Hexamine(II/III) Self-Exchange Reaction. *Phys. Chem. Chem. Phys.* **2016**, *18*, 26117–26124.
- (52) Kretchmer, J. S.; Miller III, T. F. Tipping the Balance between Concerted versus Sequential Proton-Coupled Electron Transfer. *Inorg. Chem.* **2016**, *55*, 1022–1031.
- (53) Liao, J.-L.; Voth, G. A. A Centroid Molecular Dynamics Approach for Nonadiabatic

- Dynamical Processes in Condensed Phases: The Spin-Boson Case. *J. Phys. Chem. B* **2002**, *106*, 8449–8455.
- (54) Pavese, M.; Berard, D. R.; Voth, G. A. Ab Initio Centroid Molecular Dynamics: A Fully Quantum Method for Condensed-Phase Dynamics Simulations. *Chemical Physics Letters* **1999**, *300*, 93–98.
- (55) Loose, T. D.; Sahrman, P. G.; Voth, G. A. Centroid Molecular Dynamics Can Be Greatly Accelerated through Neural Network Learned Centroid Forces Derived from Path Integral Molecular Dynamics. *J. Chem. Theory Comput.* **2022**, *18*, 5856–5863.
- (56) Paesani, F.; Voth, G. A. A Quantitative Assessment of the Accuracy of Centroid Molecular Dynamics for the Calculation of the Infrared Spectrum of Liquid Water. *The Journal of Chemical Physics* **2010**, *132*, 014105.
- (57) Paesani, F.; Voth, G. A. Nonlinear Quantum Time Correlation Functions from Centroid Molecular Dynamics and the Maximum Entropy Method. *The Journal of Chemical Physics* **2008**, *129*, 194113.
- (58) Reichman, D. R.; Roy, P.-N.; Jang, S.; Voth, G. A. A Feynman Path Centroid Dynamics Approach for the Computation of Time Correlation Functions Involving Nonlinear Operators. *The Journal of Chemical Physics* **2000**, *113*, 919–929.
- (59) Schwieters, C. D.; Voth, G. A. The Semiclassical Calculation of Nonadiabatic Tunneling Rates. *J. Chem. Phys.* **1998**, *108*, 1055–1062.
- (60) Hele, T. J. H. An Electronically Non-Adiabatic Generalization of Ring Polymer Molecular Dynamics. M.Sc. thesis, Oxford University, Oxfordshire, England, 2011.
- (61) Duke, J. R.; Ananth, N. Mean Field Ring Polymer Molecular Dynamics for Electronically Nonadiabatic Reaction Rates. *Faraday Discuss.* **2016**, *195*, 253–268.

- (62) Richardson, J. O.; Thoss, M. Communication: Nonadiabatic Ring-Polymer Molecular Dynamics. *J. Chem. Phys.* **2013**, *139*, 031102.
- (63) Menzeleev, A. R.; Bell, F.; Miller, T. F. Kinetically Constrained Ring-Polymer Molecular Dynamics for Non-Adiabatic Chemical Reactions. *J. Chem. Phys.* **2014**, *140*, 064103.
- (64) Kretchmer, J. S.; Miller III, T. F. Kinetically-Constrained Ring-Polymer Molecular Dynamics for Non-Adiabatic Chemistries Involving Solvent and Donor-Acceptor Dynamical Effects. *Faraday Discuss.* **2016**, *195*, 191–214.
- (65) Kretchmer, J. S.; Boekelheide, N.; Warren, J. J.; Winkler, J. R.; Gray, H. B.; Miller, T. F. Fluctuating Hydrogen-Bond Networks Govern Anomalous Electron Transfer Kinetics in a Blue Copper Protein. *Proc. Natl. Acad. Sci.* **2018**, *115*, 6129–6134.
- (66) Chowdhury, S. N.; Huo, P. Coherent State Mapping Ring Polymer Molecular Dynamics for Non-Adiabatic Quantum Propagations. *J. Chem. Phys.* **2017**, *147*, 214109.
- (67) Ananth, N.; Miller, T. F. Exact Quantum Statistics for Electronically Nonadiabatic Systems Using Continuous Path Variables. *J. Chem. Phys.* **2010**, *133*, 234103.
- (68) Ananth, N. Mapping Variable Ring Polymer Molecular Dynamics: A Path-Integral Based Method for Nonadiabatic Processes. *J. Chem. Phys.* **2013**, *139*, 124102.
- (69) Duke, J. R.; Ananth, N. Simulating Excited State Dynamics in Systems with Multiple Avoided Crossings Using Mapping Variable Ring Polymer Molecular Dynamics. *J. Phys. Chem. Lett.* **2015**, *6*, 4219–4223.
- (70) Pierre, S.; Duke, J. R.; Hele, T. J. H.; Ananth, N. A Mapping Variable Ring Polymer Molecular Dynamics Study of Condensed Phase Proton-Coupled Electron Transfer. *J. Chem. Phys.* **2017**, *147*, 234103.

- (71) Shushkov, P.; Li, R.; Tully, J. C. Ring Polymer Molecular Dynamics with Surface Hopping. *The Journal of Chemical Physics* **2012**, *137*, 22A549.
- (72) Tao, X.; Shushkov, P.; Miller, T. F. Path-Integral Isomorphic Hamiltonian for Including Nuclear Quantum Effects in Non-Adiabatic Dynamics. *J. Chem. Phys.* **2018**, *148*, 102327.
- (73) Tao, X.; Shushkov, P.; Miller, T. F. Simple Flux-Side Formulation of State-Resolved Thermal Reaction Rates for Ring-Polymer Surface Hopping. *J. Phys. Chem. A* **2019**, *123*, 3013–3020.
- (74) Lawrence, J. E.; Manolopoulos, D. E. An Analysis of Isomorphic RPMD in the Golden Rule Limit. *J. Chem. Phys.* **2019**, *151*, 244109.
- (75) Chandler, D. *Introduction to Modern Statistical Mechanics*; Oxford University Press: New York, 1987.
- (76) Trotter, H. F. On the Product of Semi-Groups of Operators. *Proc. Am. Math. Soc.* **1959**, *10*, 545–551.
- (77) Chandler, D.; Wolynes, P. G. Exploiting the Isomorphism between Quantum Theory and Classical Statistical Mechanics of Polyatomic Fluids. *The Journal of Chemical Physics* **1981**, *74*, 4078–4095.
- (78) Craig, I. R.; Manolopoulos, D. E. A Refined Ring Polymer Molecular Dynamics Theory of Chemical Reaction Rates. *J. Chem. Phys.* **2005**, *123*.
- (79) Ranya, S.; Ananth, N. Multistate Ring Polymer Instantons and Nonadiabatic Reaction Rates. *J. Chem. Phys.* **2020**, *152*, 114112.
- (80) Miller, W. H.; Schwartz, S. D.; Tromp, J. W. Quantum Mechanical Rate Constants for Bimolecular Reactions. *J. Chem. Phys.* **1983**, *79*, 4889–4898.

- (81) Mattiat, J.; Richardson, J. O. Effects of Tunnelling and Asymmetry for System-Bath Models of Electron Transfer. *J. Chem. Phys.* **2018**, *148*, 102311.
- (82) Henriksen, N. E.; Hansen, F. Y. In *Theories of Molecular Reaction Dynamics: The Microscopic Foundation of Chemical Kinetics*; Henriksen, N. E., Hansen, F. Y., Eds.; Oxford University Press, 2008; p 0.
- (83) Lawrence, J. Path-integral methods for non-adiabatic reaction rates. Ph.D. thesis, University of Oxford, Oxfordshire, England, 2020.
- (84) Voth, G. A. Computer Simulation of Proton Solvation and Transport in Aqueous and Biomolecular Systems. *Acc. Chem. Res.* **2006**, *39*, 143–150.